Air entrainment and free-surface fluctuations in A-type hydraulic jumps with an abrupt drop

Luo, Maoyi; Wang, Hang; Zheng, Xiaohui; Wüthrich, Davide; Bai, Ruidi; Liu, Shanjun

DOI
10.1080/00221686.2023.2239193

Publication date
2023

Document Version
Final published version

Published in
Journal of Hydraulic Research

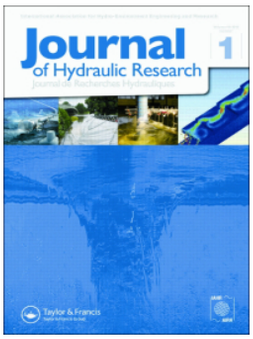

Journal of Hydraulic Research

ISSN: (Print) (Online) Journal homepage: https://www.tandfonline.com/loi/tjhr20

Air entrainment and free-surface fluctuations in A-type hydraulic jumps with an abrupt drop

Maoyi Luo, Hang Wang, Xiaohui Zheng, Davide Wüthrich, Ruidi Bai & Shanjun Liu

To cite this article: Maoyi Luo, Hang Wang, Xiaohui Zheng, Davide Wüthrich, Ruidi Bai & Shanjun Liu (2023) Air entrainment and free-surface fluctuations in A-type hydraulic jumps with an abrupt drop, Journal of Hydraulic Research, 61:5, 720-734, DOI: 10.1080/00221686.2023.2239193

To link to this article: https://doi.org/10.1080/00221686.2023.2239193

Journal of Hydraulic Research Vol. 61, No. 5 (2023), pp. 720–734
https://doi.org/10.1080/00221686.2023.2239193

Research paper

Air entrainment and free-surface fluctuations in A-type hydraulic jumps with an abrupt drop

MAOYI LUO, PhD student, *State Key Laboratory of Hydraulics and Mountain River Engineering, Sichuan University, Chengdu, PR China*
Email: luomaoyi0723@163.com

HANG WANG, Professor, *State Key Laboratory of Hydraulics and Mountain River Engineering, Sichuan University, Chengdu, PR China*
Email: hang.wang@uqconnect.edu.au

XIAOHUI ZHENG, Master Student, *State Key Laboratory of Hydraulics and Mountain River Engineering, Sichuan University, Chengdu, PR China*
Email: zhengxhscu@163.com

DAVIDE WÜTHRICH, Assistant Professor, *Faculty of Civil Engineering and Geosciences, Delft University of Technology, Delft, The Netherlands*
Email: d.wuthrich@tudelft.nl

RUIDI BAI, Associate professor, *State Key Laboratory of Hydraulics and Mountain River Engineering, Sichuan University, Chengdu, PR China*
Email: bairuidiscu@163.com (author for correspondence)

SHANJUN LIU, Professor, *State Key Laboratory of Hydraulics and Mountain River Engineering, Sichuan University, Chengdu, PR China*
Email: drliushanjun@vip.sina.com

ABSTRACT
In high dam construction projects in China, stilling basin design with an abrupt bottom drop is sometimes introduced to reduce the bottom velocity and pressure loads by generating A-type hydraulic jumps. Although the stilling basin design is not new, A-type hydraulic jumps have not been studied taking into account the air entrainment and evolution of internal air–water flow structures. This paper presents an experimental study of self-aerated A-type jumps in terms of bubble transport and free-surface fluctuations over the bottom drop. Four Froude numbers from 4.1 to 10.3 are tested for three drop heights, in addition to the flat-bottom case. Compared to the classic hydraulic jumps, A-jumps are observed with longer jump lengths and weaker free-surface fluctuations. The downward deflection of the jet-shear flow and formation of a bottom roller in the step cavity require a modification to the analytical expression of velocity and void fraction distributions. The relationship between the bubble diffusivity and jump spreading rate differs from that in classic hydraulic jumps, suggesting a faster expansion of the bubble diffusion layer than the turbulent shear flow downstream of the drop, especially for large drop heights. At large approach velocities, the reattachment of the deflected jet-shear flow to the lowered bed may cause a local rise in bubble counts downstream the bottom roller. Further increase in drop height results in a W-jump with overwhelming bottom roller over the surface roller and an arced surface jet, which is beyond the scope of this study.

Keywords: A-jump; abrupt drop; air entrainment; bottom roller; negative step;

1 Introduction

In dam projects, stilling basins are relatively expensive components designed to dissipate the high kinetic energy of the discharge flow. The energy dissipation process often takes place through a hydraulic jump (De Padova & Mossa, 2021 Hager, 1992; Wang, 2014). Hydraulic jumps are violently turbulent, rapidly varying and sometimes unsteady flow that must be

Received 21 July 2022; accepted 7 July 2023/Currently open for discussion.

ISSN 0022-1686 print/ISSN 1814-2079 online
http://www.tandfonline.com

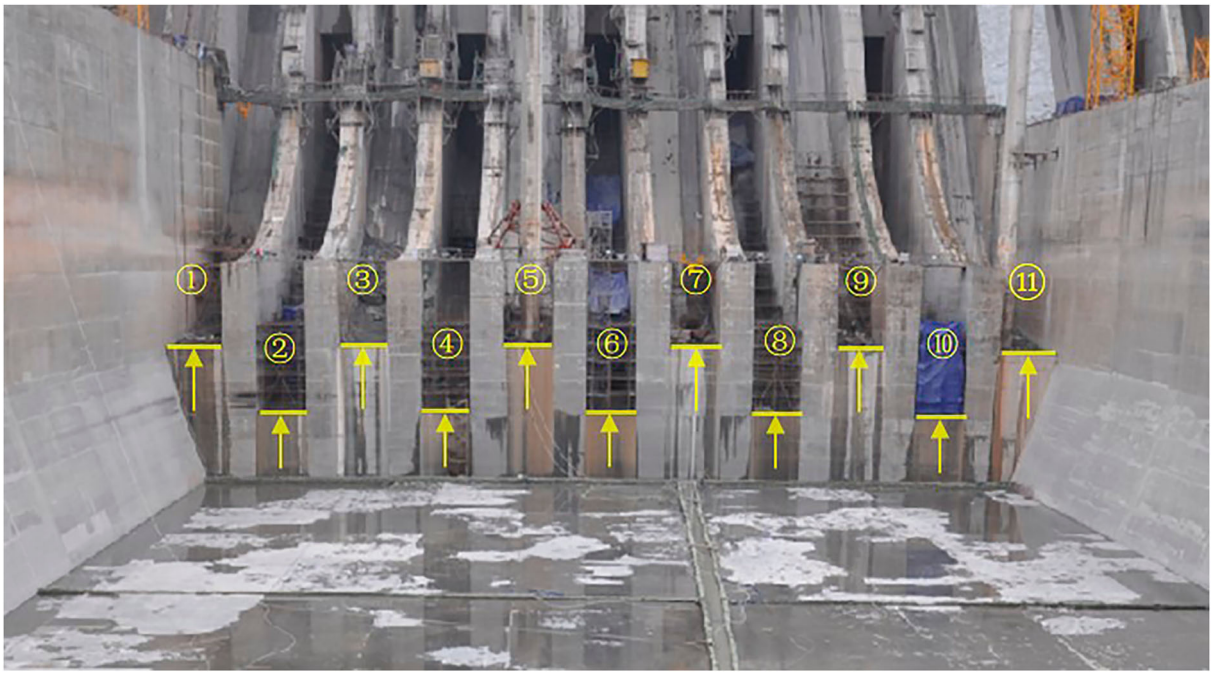

Figure 1 The Xiangjiaba Dam stilling basin with a twin-layer offset-jets inlet design, looking from downstream. The 11 spillway outlets are numbered from ① to ⑪ and the negative step edges remarked with arrows. Courtesy of Zhipan Niu. Chen et al. (2014) reported higher energy dissipation rates for a similar design based on physical modelling compared to classic hydraulic jumps and spatial B-jumps

carefully contained within the reinforced stilling basin boundaries. Even so, structural damage is occasionally recorded due to the extreme velocity and pressure fluctuations exerted upon the concrete slabs on the basin bottom. Examples include the failure of stilling basins of the Malpaso Dam in Mexico, the Karnafuli Dam in Bangladesh, and the Wuqiangxi and Jinghong Dams in China. During the construction of high dams in southwest China, a countermeasure that has been adopted to prevent stilling basin failure under the impact of high-energy discharge water is to build an abrupt drop at the entrance to the stilling basin, such as that in the Xiangjiaba Hydropower Station on the upper Yangtze River (Fig. 1) (Chen et al., 2014). The lowered stilling basin bed forms a shallow plunging pool, and the water cushion reduces the dynamic bottom-pressure load associated with the rolling motions of the hydraulic jump. The abrupt drop can also help stabilize the jump position and prevent effectively the tailwater effects (Mossa et al., 2003).

The transitional flow pattern at an abrupt drop (or negative step) is related to the inflow and tailwater flow conditions (Hager & Bretz, 1986; Moore & Morgan, 1959; Ohtsu & Yasuda, 1991). For a given inflow depth d_1 and drop height s, several types of hydraulic jumps are commonly observed as the tailwater depth d_2 decreases, namely the A-jump, the wave jump (or W-jump), the wave train, the B-jump (or maximum plunging condition), and the minimum B-jump (or limited jump) (Mossa et al., 2003 Rajaratnam & Ortiz, 1977;). Kawagoshi and Hager (1990b) investigated the positions of the wave crest and plunging point, the lengths of the jump and surface roller, and the extension of the bottom separation, for different inflow parameters of wave-type flows. Armenio et al. (2000) indicated that the maximum bottom pressure fluctuations in B-jumps were greater than those in classic hydraulic jumps (CHJs) on a flat bed, with possible pressure coefficient exceeding unity, while those in W-jumps were smaller. Ferreri and Nasello (2002) and Ohtsu and Yasuda (1991) provided physical explanations for the changes in hydraulic jump flow patterns and characteristics due to the bottom drop, the former being based on comparative observation of the phenomenon at sudden cross-sectional enlargement, and the latter highlighting the significance of the dimensionless drop height s/d_1, in agreement with the finding of Kawagoshi and Hager (1990a). Mossa et al. (2003) described the occurrence of quasi-periodic oscillatory flow conditions between two different jump types over long-lasting experiments. Their experimental observations of cyclic formation and evolution of jump vortices were successfully reproduced by De Padova et al. (2018) using SPH modelling. All physical model studies focused on the flow pattern and hydraulic characteristics of the various types of hydraulic jump flow at drops, and none has considered the development of internal air–water flow or detailed roller fluctuations. This has prevented systematic comparative analysis and understanding of the two-phase flow processes in hydraulic jumps at drops with reference to the well documented CHJs.

Specifically, for an A-jump with the jump toe located upstream the step edge followed by an established surface roller over the step, it is generally understood that a greater energy dissipation rate can be achieved compared to a CHJ without bottom offset, while similar transitional flow patterns are visibly exhibited. Air–water flow properties that have been extensively investigated for CHJs included maximum free-surface fluctuation

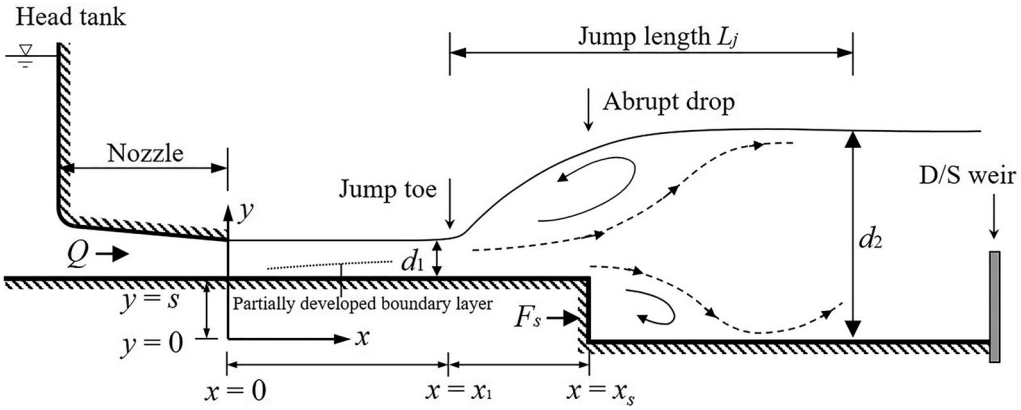

Figure 2 Definition sketch of A-type hydraulic jump at an abrupt drop. The facility is two-dimensional, of the same geometry across the flume width

magnitude, frequency and position, distributions of void faction, bubble count rate and velocity, bubble size spectrum and bubble clustering, among others, usually with additional focuses on the effects of inflow conditions (e.g. Chanson, 2010, 2011; De Padova & Mossa, 2021; Felder et al., 2021; Gualtieri & Chanson, 2007, 2021 Montano & Felder, 2021; Wang, 2014; Wang & Chanson, 2015; Wüthrich et al., 2022). In this paper, some of these parameters are studied for A-jumps at a variety of inflow Froude numbers F_1 and relative drop heights s/d_1, where $\mathsf{F}_1 = V_1 g^{-0.5} {d_1}^{-0.5}$, $V_1 = Q/(Wd_1)$, Q is the flow rate and W the width of rectangular channel, and g is the gravity. The free-surface and air–water flow characteristics are comparatively analysed with reference to CHJs of identical inflow conditions, and the influence of the drop on the air–water flow properties is revealed.

2 Experimental set-up and flow conditions

The experimental facility consisted of a head tank (2.5 × 2.5 m^2 in area and 1.7 m in height) and a horizontal rectangular channel (5.0 m in length, 0.4 m in width and 0.5 m in height) made of high-density polyethylene bottom and glass sidewalls. Water was pumped from an underground reservoir into the head tank and then discharged into the channel through a gradually convergent jet-box nozzle with a horizontal invert (0.6 m in length, 0.4 m in width) and rectangular cross-section. The nozzle outlet opening height was 0.02 m at the longitudinal position $x = 0$. The bottom of the initial 0.7-m-long open channel section ($0 < x < 0.7$ m) was the extension of the nozzle invert, ending with an abrupt drop at $x_s = 0.7$ m (Fig. 2). The downstream channel bed ($0.7\text{ m} < x < 5.0\text{ m}$) was lowered by the drop height s. The zero of the vertical coordinate $y = 0$ was defined at the downstream bed level, thus the invert of the upstream approach flow was at $y = s$. The tailwater level was controlled by a sharp-crested weir at the channel outlet. The outflow was collected in a recirculating channel leading to the reservoir, where the flow rate Q was measured using a V-notch weir with an accuracy of 1%.

A-type hydraulic jumps were generated with the oscillating jump toe being located around a mean position $x_1 = 0.52$ m, i.e. 0.18 m upstream the step edge. The visual determination of the mean jump toe position might introduce some uncertainty in the relative distance from the jump toe to a downstream measuring point x–x_1, leading to data scattering. The clear-water inflow depth d_1 was measured using a pointer gauge with a practical accuracy of 0.5 mm. For the fixed jet-box nozzle opening and developing length of the approach flow, $d_1 = 0.023$ m for all tested flow rates and inflow Froude numbers $4.1 < \mathsf{F}_1 < 10.3$, where the boundary layer was partially developed. Four different drop heights were investigated, including $s = 0$ for the flat bed configuration. The corresponding dimensionless drop height was $s/d_1 = 0$, 0.87, 1.74 and 3.48, respectively, classified as low drops according to Ohtsu and Yasuda (1991). A further enlarged drop height $s/d_1 = 6.96$ was also tested for simple flow visualization without detailed air–water flow measurement, as the flow could not maintain the A-jump form (see the following section). Table 1 lists the experimental flow conditions, where d_2 was derived from the ADM readings, the Reynolds number $\mathsf{R}_1 = V_1 d_1/\nu$, the Weber number $\mathsf{W} = \rho {V_1}^2 d_1/\sigma$, ν = the kinematic viscosity of water, and σ = the air–water surface tension.

3 Instrumentation

The fluctuating free-surface elevations above the invert η were measured with a down-looking acoustic displacement meter (ADM, Microsonic™ Mic + 25/IU/TC, Dortmund, Germany) along the channel centreline. The ultrasonic sensor provided a measurement range between 0.03 and 0.35 m from the sensor head. It was sampled at 100 Hz for 180 s at a given position. Given proper zeroing of the ADM elevation above the channel bed, accurate free-surface detection can be achieved for a well-defined air–water interface with an error less than 0.5 mm. However, for the highly turbulent and breaking jump roller surface, systematic error up to 2 mm may exist as a result of the acoustic beam penetrating through the foamy air–water interfacial layer

Table 1 Experimental flow conditions: for the test number T#, # = 1 for s = 0 m, # = 2 for s = 0.02 m, # = 3 for s = 0.04 m, # = 4 for s = 0.08 m

Test	Q (m^3 s^{-1})	x_1 (m)	d_1 (m)	x_s(m)	S (m)	V_1 (m s^{-1})	d_2 (m)	F_1	R_1 ($\times 10^5$)	W
T#-1	0.0178	0.52	0.023	0.7	0 / 0.02 / 0.04 / 0.08	1.93	0.126	4.1	0.45	1156
T#-2	0.0267					2.90	0.192	6.1	0.67	2611
T#-3	0.0334					3.63	0.240	7.6	0.83	4083
T#-4	0.0450					4.90	0.317	10.3	1.13	7465

(Zhang et al., 2018). In addition, the uncertainty in measuring the free-surface fluctuation was also affected by the selection of ADM signal cleaning method. In this study, the erroneous points in the signal due to missing reflection on the severely curved air–water interface or splashing contamination were filtered using the robust outlier cutoff method, where the cutoff threshold was determined by the sample size (Valero et al., 2020). The free-surface elevation and its fluctuation were characterized with the median and median absolute deviation of the filtered samples, as the classic free-surface turbulence estimator like the mean and standard deviation may not be sufficient for such highly turbulent two-phase flow (Valero et al., 2020). Introduction of further robust filtering methods could potentially increase the accuracy of outlier elimination and reduce the signal deviation by up to 5%.

The void faction C and bubble count rate F of the aerated flow were measured using a dual-tip conductivity probe manufactured at Sichuan University. The phase-detection needle sensors had a 0.1-mm tip diameter and a 0.8-mm outer diameter. The two sensors were separated by 2 mm side by side, and the trailing tip was 10 mm behind the leading tip against the approach flow direction. The sensors were excited simultaneously and sampled at 40 kHz for 45 s at each measuring point. The time-averaged void fraction and bubble count rate were derived from the binarized signal in which 0 stood for water and 1 for air. The binarization of the raw signal adopted a 50% threshold between the most probable air and water voltage levels (Chanson, 2002). A cross-correlation between the raw signals of the two tips provided the average interfacial travel time between the tips, thus the velocity component V_x along the sensor direction (Crowe et al., 1998). A further screening of the uncorrelated signal segments due to severe flow-sensor misalignment, as introduced by Kramer et al. (2019), was applied to the velocity calculation (specifically, by setting each signal segment containing a number of $N_p = 15$ bubbles and a screening criterion parameter $A = 0.3$ as defined in Kramer et al. (2020)). The accuracy of bubble detection is related to the bubble–sensor interaction and was maximized in the experiments by sharpening the sensor tips. Uncertainties in the derivation of void fraction, bubble count rate and bubble velocity were subject to the selection of the key data processing parameters including the binarization threshold, signal segment size and correlation screening criterion, in addition to the total number of detectable bubbles. Longer sampling duration should be recommended to minimize the influence of the oscillating jump toe motions on the measurement and maximize the measurement repeatability, although all convergent results were obtained using the present measuring time. Despite the data scattering due to the combining effects of these factors, possible errors of 5% may be expected empirically for the determination of void fraction and bubble count rate, while an uncertainty up to 10% is deemed acceptable for the velocity calculation, as long as a proper data retention rate is guaranteed after the correlation-based data cleaning. The vertical elevation of the probe was controlled with a Vernier calliper on the translating mechanics with an accuracy of 0.1 mm.

4 Flow pattern and free-surface characteristics

The A-jumps were generated over relatively small drop heights compared to the downstream depth d_2, and the drop in bottom elevation did not prevent the formation of the surface roller between the sections of d_1 and d_2. Despite the sudden bottom drop below the surface roller and the increase in flow depth, the overall air–water flow appearance was not remarkably different from a CHJ at first glance. Sideview observations indicated that the key difference between an A-jump and a CHJ was a downward deflection of the jet-shear flow over the negative step and the formation of an additional bottom roller in the step cavity, as sketched in Fig. 2. Detailed comparison of the internal flow structures due to the presence of the bottom drop is presented in the following sections. For constant inflow conditions upstream of the step, a further increase in the drop height would lead to a transition from A-jump to W-jump. Please see this additional information in the Appendix.

This study was focused on the A-jumps. For a given F_1, visual observation indicated that the relative tailwater surface elevation above the approach flow level (d_2-s-d_1) reduced with increasing drop height. This is demonstrated in Fig. 3 with the time-averaged free-surface profiles for $F_1 = 10.31$ and different drop heights s/d_1. The corresponding free-surface fluctuations are discussed later. The mean depth d_2 above the stilling basin bed was recorded and the conjugate depth ratio d_2/d_1 is presented in Fig. 4 for all tested F_1 and s/d_1. Ignoring the friction resistance, the conservation of momentum suggests:

$$P_1 + M_1 + P_s = P_2 + M_2 \quad (1)$$

where P_1, P_2 and M_1, M_2 are the integral pressures and momentum fluxes at the upstream and downstream sections of the jump,

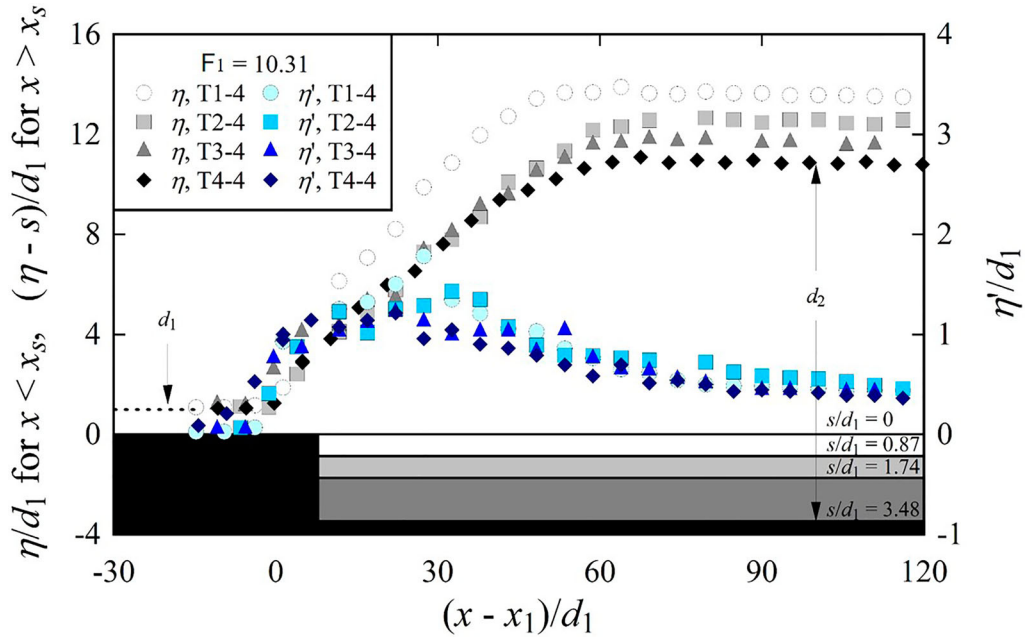

Figure 3 Developments of mean free surface level free surface fluctuations from upstream the jump toe to far field region

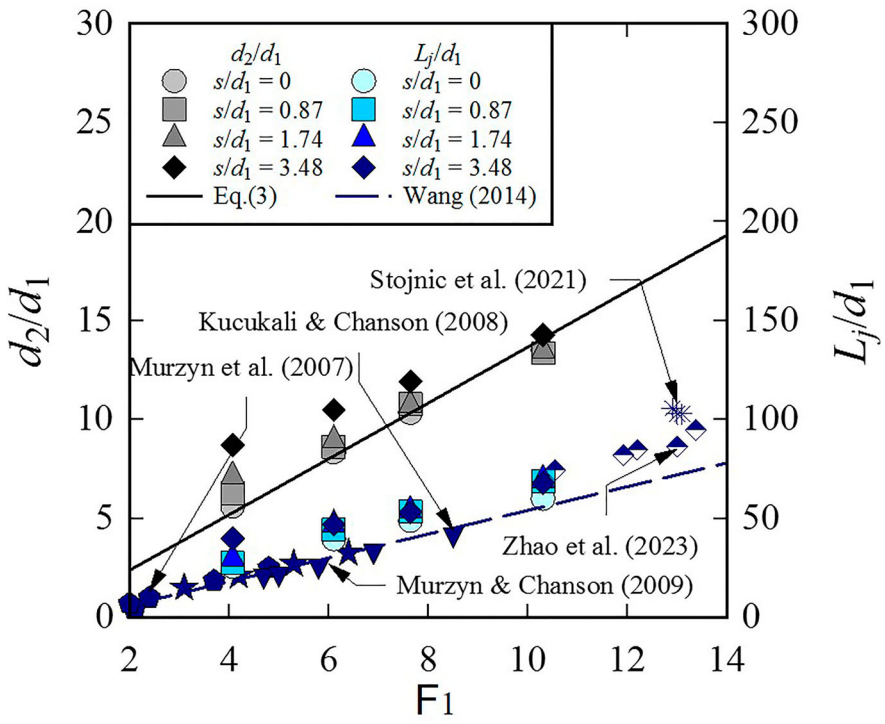

Figure 4 Conjugate depth ratio and dimensionless jump length as functions of inflow Froude number for different drop heights; literature jump length data obtained in CHJs

respectively, and P_s equals the integral pressure on the vertical drop surface. The solution of the momentum and continuity equations yields:

$$\mathsf{F}_1^2 = \frac{d_2}{2d_1}\left[d_1 + d_2 - \frac{2P_s}{d_1(d_2 - d_1)}\right] \tag{2}$$

When $P_s = 0$, Eq. (2) becomes the classic Bélanger equation:

$$\frac{d_2}{d_1} = \frac{1}{2}\left(\sqrt{1 + 8\mathsf{F}_1^2} - 1\right) \tag{3}$$

Equation (2) implies that the conjugate depth ratio d_2/d_1 increases with increasing drop height for a given F_1, thus

achieving a greater energy dissipation rate. This is supported by the present data in Fig. 4, where the difference in d_2/d_1 between different drop heights becomes more evident at small Froude numbers (i.e. when the relative drop height to downstream depth s/d_2 is larger).

The mean free-surface profiles enabled quantification of the jump length L_j defined as the longitudinal distance from the jump toe to the downstream section where constant d_2 was first reached with a quasi-horizontal free-surface. The dimensionless jump length L_j/d_1 is also plotted in Fig. 4. Comparison between the present CHJ data ($s = 0$) and the data of Murzyn et al. (2007), Kucukali and Chanson (2008) and Murzyn and Chanson (2009), as well as the empirical equation $L_j/d_1 = 6(\mathsf{F}_1–1)$ proposed by Wang (2014), indicates slightly greater L_j observations in our experiments, because they defined the end of L_j at the section where $\partial\eta/\partial x = 0$ was reached, while in all studies the spatial resolution allowed for uncertainties in L_j estimation. The two definitions are identical when the depth increases monotonically from d_1 to d_2 over the jump length. However, a high-spatial-resolution free-surface scanning usually captures a maximum depth ($\partial\eta/\partial x = 0$) first and a constant d_2 at a slightly downstream position, as visible in Fig. 3 for T1–4 ($s/d_1 = 0$), resulting in a larger L_j. The data documented by Stojnic et al. (2021) and Zhao et al. (2023) at the maximum depths of pre-aerated hydraulic jumps preceded by sloping chutes appeared to be comparatively larger in a range of greater F_1. For $s/d_1 > 0$, Fig. 3 shows a flattening of the roller front and a reduction of the jump slope or steepness defined as $\alpha = \tan^{-1}[(d_2\text{-}s\text{-}d_1)/L_j]$. The decreasing α with increasing s/d_1 is associated with both reduction in the relative tailwater level $d_2\text{-}s\text{-}d_1$ and increasing jump length L_j (Fig. 4).

Figure 3 also shows the longitudinal evolution of dimensionless free-surface fluctuation magnitude η'/d_1 represented by the standard deviation of the ADM samples. The first half of the jump length was characterized by relatively high surface fluctuations, due to both up-and-down depth variations and back-and-forth jump toe oscillations. A maximum fluctuation η'_{max}/d_1 occurred at similar positions downstream of the jump toe. Further downstream, η'/d_1 decreased gradually to some constant levels in the far-field zone as surface waves propagated down the tailwater. Figure 5 shows increasing maximum fluctuations η'_{max}/d_1 with increasing F_1, as indicated in the literature (Felder et al., 2021 Wang & Chanson, 2015;). The data for $s/d_1 = 0$ compared well with the data of Murzyn et al. (2007), Kucukali and Chanson (2008), Murzyn and Chanson (2009), Zhao et al. (2023) and the correlation of $\eta'_{max}/d_1 = 0.15(\mathsf{F}_1–1)$ in Wang (2014), all for partially-developed inflow conditions. For a given F_1, η'_{max}/d_1 decreased with increasing drop height s/d_1. A lowered bed, reduced jump front steepness and the bottom water cushion helped jointly reduce the free-surface turbulence. In addition, the rolling motion in the step cavity is assumed to add to the kinetic energy dissipation, contributing to a greater d_2 and reduced surface roller fluctuations as well.

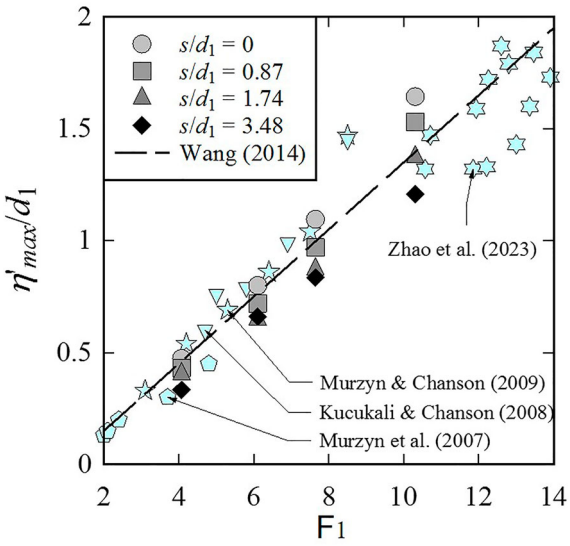

Figure 5 Maximum free-surface fluctuations as a function of inflow Froude number for different drop heights; literature jump length data obtained in CHJs

5 Air entrainment and bubble transport

The appendix shows an average streamline distribution over an 8-s imaging duration. For the largest drop height and Froude number (Experiment T4-4), Fig. 6 further presents the distributions of the longitudinal interfacial velocity V_x/V_1 measured with the conductivity probe over the 45-s period, at seven vertical cross-sections. The characteristic position y_{90} where $C = 0.9$ is outlined. The typical wall-jet velocity distributions were reproduced upstream of the drop edge ($x_1 < x < x_s$), as documented in the literature for CHJs. The S-shaped velocity profile exhibits a maximum jet velocity V_{max} at a vertical position y_{Vmax} and negative velocity in the upper surface roller. For $x > x_s$, the jet layer was deflected downward and the position y_{Vmax} shifted towards the lowered bed. It should be noted that only velocities in the x direction were captured by the conductivity probe and the downward component was not measured. Negative horizontal velocity was detected in the bottom roller region behind the step. It is important to point out that the accuracy of negative velocity measurement could be reduced by the regular probe position, and a reversed probe with the sensors pointing downstream should be considered in the lower bottom roller, which was unfortunately restricted by the size of the probe tube in the present experiments. The sudden bottom drop also caused an expansion of the surface roller thickness and elongated the reversing free-surface flow section. Beyond the end of the surface roller, the velocity profile exhibited some transitional shape from the wall-jet form to that of a uniform open-channel flow.

In Fig. 6, the velocity data for $x_1 < x < x_s$ and downstream of the bottom roller fit well the theoretical velocity distribution

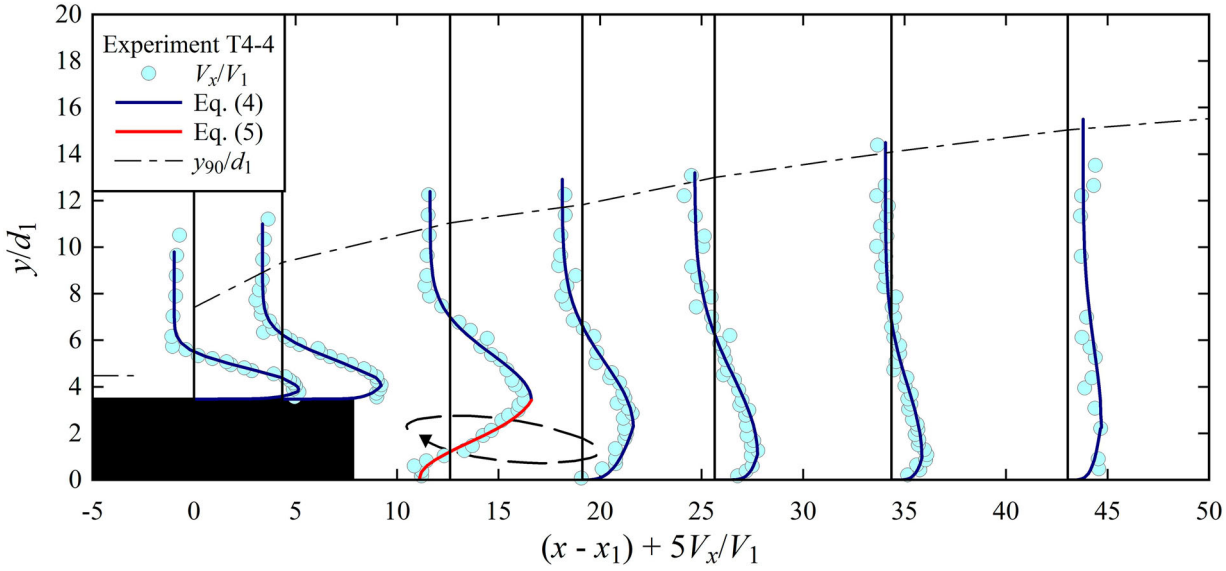

Figure 6 Experimental data and theoretical profiles of longitudinal interfacial velocity distributions for experiment T4-4

(Chanson, 2010):

$$\frac{V - V_{fs}}{V_{max} - V_{fs}} = \exp\left(-\frac{1}{2}\left(1.765\frac{y - y_{V_{max}}}{y_{0.5}}\right)^2\right) \quad \text{for } y > y_{V_{max}} \tag{4–1}$$

$$\frac{V}{V_{max}} = \left(\frac{y}{y_{V_{max}}}\right)^{\frac{1}{N}} \quad \text{for } y < y_{V_{max}} \tag{4–2}$$

where V_{fs} is the average velocity across the upper free-surface region, $V_{fs} < 0$ within the surface roller section and $V_{fs} > 0$ at further downstream, and $y_{0.5}$ is the vertical position where $V = (V_{max} + V_{fs})/2$. It was noted that the introduction of the aforementioned correlation screening processing improved the accuracy of determining V_{fs} magnitude and $y_{0.5}$ position from the data measured in the regions with highly varying instantaneous velocity directions, thus increasing the accuracy of Eq. (4–1) on velocity profile reproduction. The velocity in the bottom boundary layer was approximated with the power-law equation, where $N > 7$ was typically found for $x < x_s$ when the near-bottom flow was highly aerated and $N < 6$ at downstream of the bottom roller. With the presence of the bottom roller, the velocity profile is expressed by replacing Eq. (4–2) with Eq. (5):

$$\frac{-V - V_{max}}{V^b_{max} - V_{max}} = \exp\left(-\frac{1}{2}\left(1.765\frac{y - y^b_{V_{max}}}{y^b_{0.5}}\right)^2\right) \quad \text{for } y < y_{V_{max}} \tag{5}$$

where $V^b_{max} < 0$ is the local peak reversing velocity in the bottom roller at $y = y^b{}_{Vmax}$, and $V = (V_{max} + V^b{}_{max})/2$ at $y = y^b{}_{0.5}$. Equation (5) applies to the bottom roller region whose length was found to be shorter than that of a simplistic parabolic jet trajectory over a drop height h_s. The boundary layer velocity within the bottom roller could not be captured accurately with the probe owing to the low bubble density and the sensor-streamline misalignment.

The transport of entrained air bubbles in the mixing shear layer was also modified by the flow expansion and streamline diversion over the abrupt drop. The distributions of void fraction are presented in Fig. 7 for the same flow conditions as in Fig. 6. The data in the cross-sections upstream and downstream of the bottom roller region are compared with the theoretical equation as a combination of the bell-shaped void fraction distribution in the jet-shear region on the bottom (the first term on the right-hand side of Eq. (6)) and the monotonically increasing distribution across the surface roller region on the top (the second term on the right-hand side of Eq. (6)):

$$C = C_{max}\exp\left(-\frac{1}{4D_\#}\frac{\left(\frac{y - y_{Cmax}}{d_1}\right)^2}{\frac{x - x_1}{d_1}}\right) + \frac{1}{2}\left(1 + \text{erf}\left(\frac{1}{2D_*}\frac{\frac{y - y_{50}}{d_1}}{\sqrt{\frac{x - x_1}{d_1}}}\right)\right) \tag{6}$$

where C_{max} is the local maximum void fraction in the jet-shear layer, y_{Cmax} is the vertical position of C_{max}, y_{50} is the vertical position of $C = 0.5$ in the free-surface region, $D_\#$ and D_* are the equivalent mean dimensionless diffusivities of air bubbles in the jet-shear and free-surface regions, respectively, and erf() denotes the Gaussian error function. Note that Eq. (6) is not valid at the jump toe with $(x\text{-}x_1)/d_1 = 0$, which is a singular point of air entrainment, although a void fraction profile with comparable shape was obtained because of the jump toe oscillations over this point.

In the bottom roller area behind the negative step, a secondary maximum void fraction $C^b{}_{max}$ was shown in the roller core (Fig. 7), as a result of air bubbles entering the step cavity

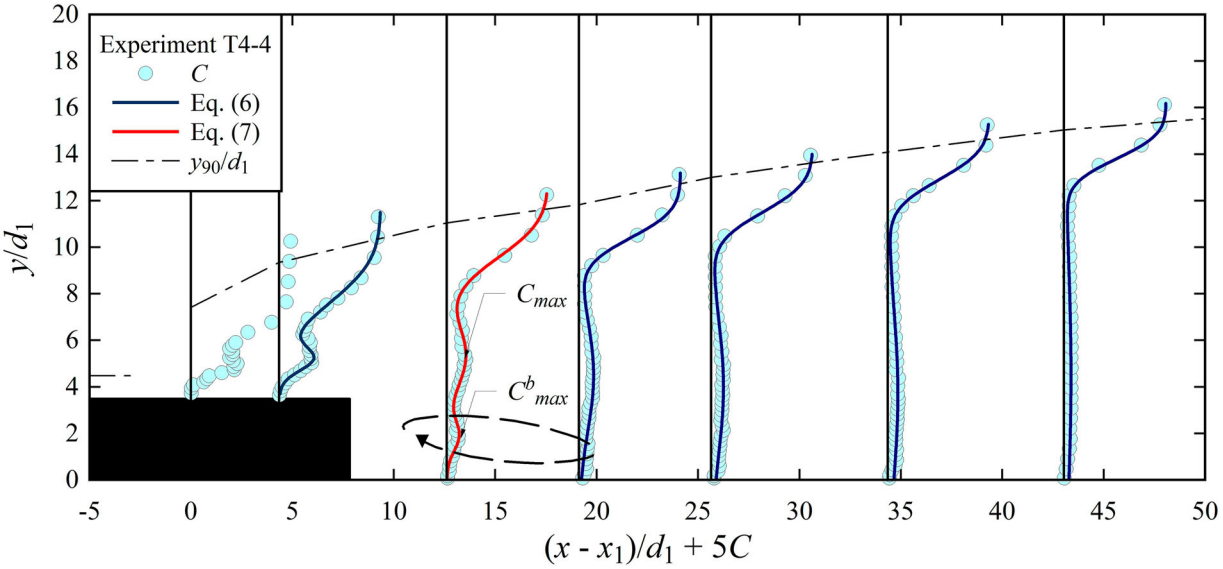

Figure 7 Experimental data and theoretical profiles of void fraction distributions for experiment T4-4

from the downward-deflected air–water shear flow and being trapped in the roller by the centrifugal force. Assuming the cross-sectional bubble distribution in the enclosed bottom roller also follows the solution of the advective diffusion equation for air bubbles (physically this is not necessarily valid), the void fraction profile in this section can be modified to:

$$C = C^b_{\max} \exp\left(-\frac{1}{4D^b_{\#}} \frac{\left(\frac{y-y^b_{C\max}}{d_1}\right)^2}{\frac{x-x_1}{d_1}}\right) + C_{\max} \exp\left(-\frac{1}{4D_{\#}} \frac{\left(\frac{y-y_{C\max}}{d_1}\right)^2}{\frac{x-x_1}{d_1}}\right) + \frac{1}{2}\left(1 + \text{erf}\left(\frac{1}{2D_*} \frac{\frac{y-y_{50}}{d_1}}{\sqrt{\frac{x-x_1}{d_1}}}\right)\right) \quad (7)$$

where $y^b{}_{C\max}$ is the vertical position of $C^b{}_{\max}$ in the bottom roller and $D^b{}_{\#}$ is the local diffusion coefficient.

The void fraction distributions in Fig. 7 demonstrate the rapid broadening of the air–water shear layer downstream the drop and the decreasing $C_{\max}$ with increasing longitudinal distance from the jump toe. Figure 8a shows the longitudinal decay in $C_{\max}$ for all tested drop heights under three Froude numbers, and the data of depth-averaged void fraction C_{mean} are presented in Fig. 8b, where:

$$C_{mean} = \frac{1}{y_{90}} \int_0^{y_{90}} C dy \quad (8)$$

The three groups of data with different colour darkness correspond to the three different Froude numbers, showing remarkably different slopes for the reduction of $C_{\max}$ and C_{mean} along the jump, as a result of the predominant effects of F_1 on the air entrainment and detrainment. For a given F_1 (i.e. among the data of similar reduction slopes), the difference in $C_{\max}$ between the various drop heights was little, and their deviation from the reference values in CHJs was practically negligible. The present data agree well with the empirical correlation by Wang and Chanson (2016) based on CHJ experiments:

$$C_{\max} = 0.5 \exp\left(-\frac{1}{1.8(\mathsf{F}_1 - 1)} \frac{x - x_1}{d_1}\right) \quad (9)$$

as shown in Fig. 8a. The minor deviation in the downstream low-air-content sections was related to both prediction and measurement uncertainties. Their fitting of the mean void fraction C_{mean} is also compared with the present data in Fig. 8b:

$$C_{mean} = 0.45 \exp\left(-\frac{1}{3.33(\mathsf{F}_1 - 1)} \frac{x - x_1}{d_1}\right) \quad (10)$$

Unlike the local maxima, the depth-averaged values C_{mean} in A-jumps were found to decrease with increasing drop height s/d_1 under the same F_1, because of the increasing conjugate depth. In addition, as shown above, the free-surface fluctuations attenuated with increasing drop height, which reduced the contribution of the air–water exchange through the breaking surface to the calculation of C_{mean} up to $y = y_{90}$.

Figure 8c and d further compare respectively the longitudinal variations of the vertical position $y_{C\max}/d_1$ for different bottom configurations, under the specified Froude numbers. Linear-like rise of $y_{C\max}/d_1$ was observed in the reference CHJ cases, consistent with the results of Wang and Chanson (2016) and other literature. In A-jumps, the $y_{C\max}/d_1$ elevation shifted downwards behind the drop. For the larger s/d_1 and F_1 cases (e.g. T3-4 and T4-4 in Fig. 8d), it is clearly seen that the position $y_{C\max}/d_1$

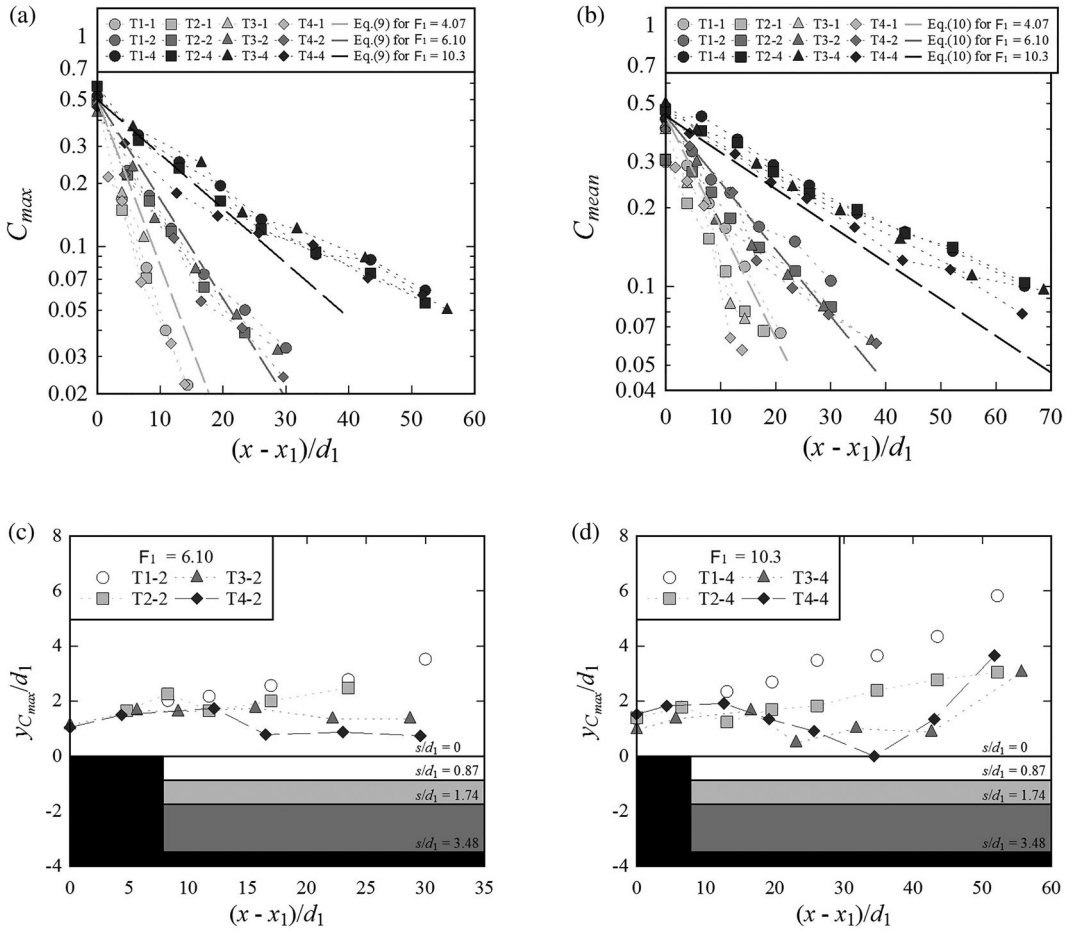

Figure 8 Longitudinal variations of characteristic void fraction quantities for different drop heights and Froude numbers: (a) maximum void fraction in the jet-shear region; (b) depth-averaged void fraction; (c) & (d) dimensionless elevation of C_{max}

first reduced over the bottom roller section before the subducting flow impacted the bed, then it increased gradually as the advected bubbles diffused and rose in the far-field region.

The mean bubble diffusivity $D_{\#}$ in Eq. (6) reflects the broadening of the air diffusion layer that originates from the jump toe. Figure 9a shows the longitudinal increase of $D_{\#}$ deriving from the best data fit for all tested flow conditions. Although the diffusivity is also a function of F_1, we focused in this work on the effects of the drop height s/d_1 and grouped the data of different F_1 for the same bed configuration in Fig. 9. A comparison shows good agreement between the present CHJ data and the prediction of Wang (2014) for $\mathsf{F}_1 = 10.3$. When the drop height increased, greater $D_{\#}$ was obtained as the air–water shear layer expanded with the increasing depth. In a hydraulic jump, the expansion of the air diffusion layer was accompanied by the expansion of the turbulent shear layer. The spreading rate of the shear layer can be characterized with the vertical distance from the channel bed to the position $y_{0.5}/d_1$ where the theoretical velocity gradient is maximum. The radio $D_{\#}/(y_{0.5}/d_1)$ thus characterizes the relative expansion of the air diffusion layer to the velocity shear layer. The results are compared in Fig. 9b between different drop heights. For CHJs with $s/d_1 = 0$, an almost constant ratio $D_{\#}/(y_{0.5}/d_1) \approx 0.0162$ was obtained along the jump for all tested F_1, with a standard deviation of 0.0022 (marked with the cyan band in Fig. 9b). This trend was remarkably changed in the A-jumps, showing increasing $D_{\#}/(y_{0.5}/d_1)$ with increasing distance over the length of the jump. The increasing rate was larger for a larger drop height. The increasing tendency is approximated in Fig. 9b with the dash line, although the trend would strictly speaking be a function of s/d_1. This finding suggested that an abrupt drop caused a faster expansion of the bubble diffusivity in the normal direction than the simultaneous expansion of the turbulent shear layer over the lowered invert. This corresponded to the fact that the flow velocity in the -y direction and the bottom roller assisted with the downward transport of the air bubbles, which enhanced the air–water mixing through the hydraulic jump.

Figure 10 presents the bubble count rate distributions for Experiment T4-4. The maximum bubble count rate F_{max} in the jet-shear layer was well captured at all cross-sections as the result of intensive bubble breakup by turbulence. For $x > x_s$, the vertical position of F_{max} also followed the downward bubble transport to decrease towards the lowered bed, as illustrated by the blue arrows. A secondary local peak bubble count rate was detected within the bottom roller, although its magnitude

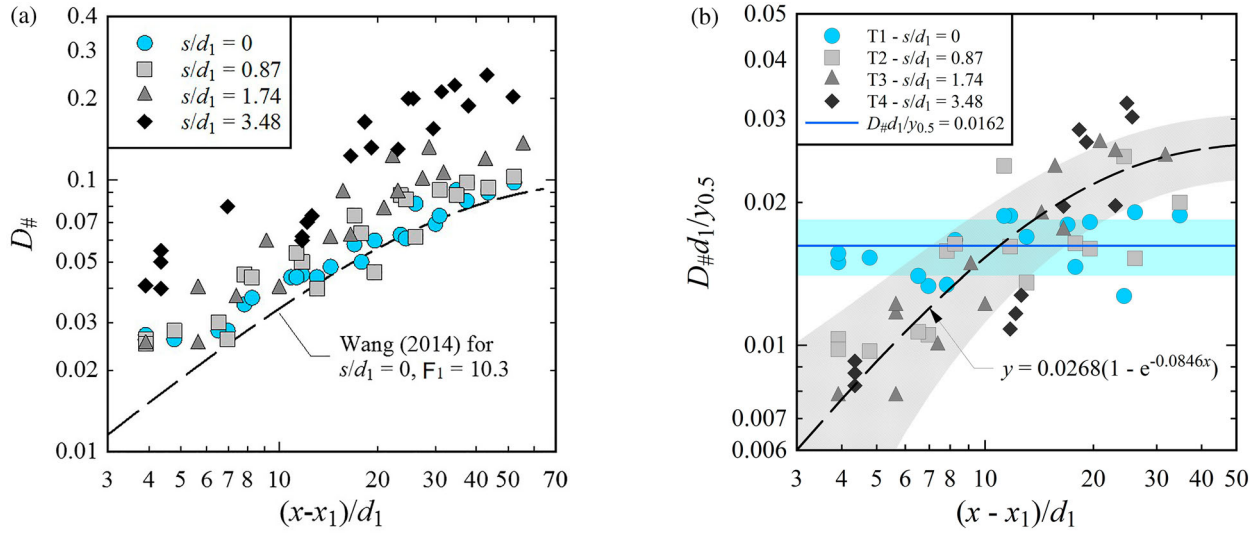

Figure 9 Bubble diffusivity $D_\#$ in jet-shear region for different drop heights: (a) longitudinal increase in $D_\#$; (b) ratio of bubble diffusivity to jump spreading rate $D^\#/(y_{0.5}/d_1)$; the dash line approximates the increasing trend for the present combined datasets with $s/d_1 > 0$, and the shadowed band shows the fitting error

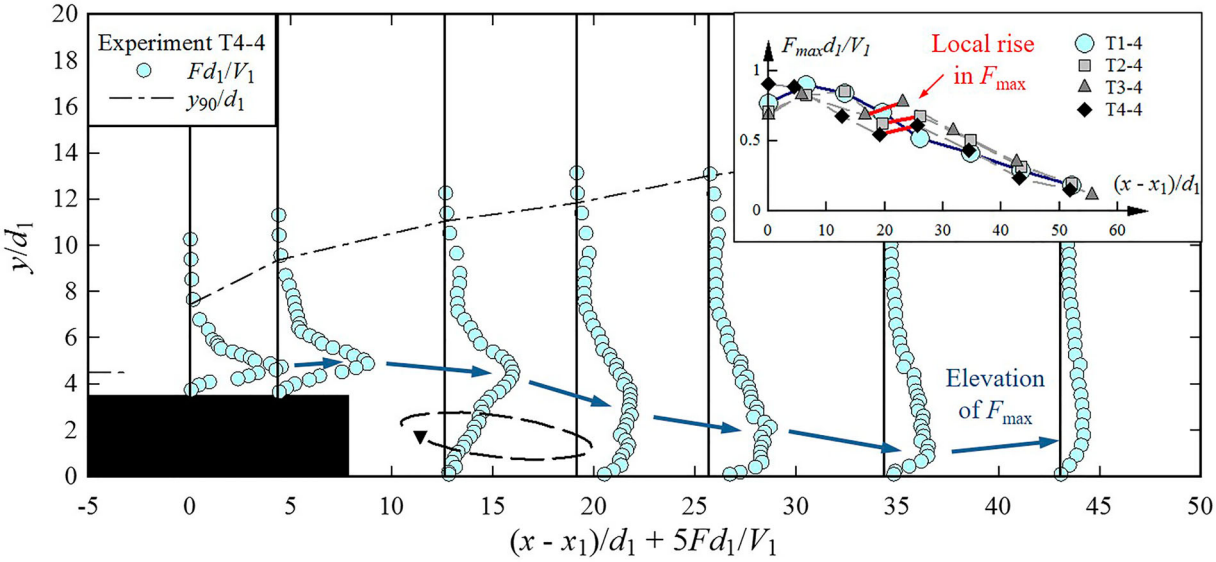

Figure 10 Dimensionless bubble count rate distributions for experiment T4-4 and longitudinal variation of dimensionless maximum bubble count rate F_{max} for $F_1 = 10.31$ (in the small window); blue arrows show the change in elevation of F_{max} and red lines show the local rise in F_{max} downstream the bottom roller

was unreliable due to the bubbles approaching from the rear of the probe sensors. For CHJs, F_{max} typically experiences a rapid rise at the jump toe and reduces monotonically along the jump, as the bubbles diffuse and the shear layer de-aerated. This was observed in the present experiments only for the smaller Froude numbers. However, for $F_1 = 10.31$, a local increase in F_{max} was seen for all drop heights downstream the end of the bottom roller, where the downward-deflected flow reattached to the channel bed (see the small window on the top right of Fig. 10). This is a similar phenomenon to the one observed during the impact of a self-aerated free-falling jet over a negative step on the downstream solid channel bed, where the entrained bubbles in the jet are broken into a greater number of smaller bubbles at the jet impact point by the sudden increasing pressure and shear forces, leading to an increasing bubble count rate (Toombes & Chasnson, 2007; Wang et al., 2021). In an A-jump, the jet is basically submerged, and its kinetic energy is largely absorbed by the bottom roller and surface roller, leaving a small impact velocity at the jet reattachment point. Therefore, the additional bubble breakup at the jet reattachment point was minor, even for the largest Froude number tested in this study, and the relative increase in F_{max} was insignificant.

6 Discussion

Both hydraulic jumps and plunging jets are commonly employed as energy dissipators by high dams. The former takes the advantage of causing less atomization thus reducing the risk

Table 2 Examples of dams equipped with negative-stepped stilling basin design (some are in construction)

Dam	Country	River	Height of dam (m)	Drop height (m)
Tehri	India	Bhagirathi River	260.0	3.5
Sayano-Shushenskaya	Russia	Yenisei River	242.0	4.2–6.0
Mong Ton	Myanmar	Salween River	227.5	–
Guandi	China	Yalong River	168.0	6.5
Xiangjiaba	China	Jinsha River	161.0	8.0–9.0
Jin'anqiao	China	Jinsha River	160.0	–
Guanyinyan	China	Jinsha River	159.0	7.5
Liyuan	China	Jinsha River	155.0	15.78
Myitsone	Myanmar	Irrawaddy River	139.5	–
Tingzikou	China	Jialing River	116.0	8.0

of bank slope failure for mountain-valley rivers. However, even for a moderate water head of 60 m, the stilling basin bed below the hydraulic jump can face a large near-bottom velocity over 30 m s^{-1}, challenging the structural strength. An increasing number of stilling basin designs have adopted the negative-stepped bottom configuration to reduce the near-bottom velocity. Some examples are shown in Table 2. Taking the Jin'anqiao Dam for instance, with an entrance flow velocity of 35 m s^{-1}, lowering the stilling basin bed by 6 m from the entrance level was able to reduce the maximum near-bed velocity from 26.4 m s^{-1} to 12.4 m s^{-1}. The reduction of the bottom shear stress may be affected by the air bubble distribution in the near-bottom region. Another key factor affecting the structural endurance is the fluctuating pressure load exerting on the stilling basin bed (Bowers & Toso, 1990). The bottom pressure fluctuations can be also modified by the aeration process due to the change in fluid density and compressibility. Therefore, future studies should be carried out by taking proper consideration of the air–water flow.

In physical studies involving air–water flow processes, the effect of model downscaling on air entrainment and bubble transport is a critical concern. The negative-stepped stilling basin model in this study represents typically a 1:40 to 1:100 downsized model, depending on the scale of prototype structure and flow condition. The model Reynolds numbers and Weber numbers are given in Table 1. While a Froude similitude may guarantee relatively accurate modelling of the flow dimensions including the sizes of both surface and bottom rollers, the flow turbulence and its interplay with air bubble breakup, water droplet ejection, and free-surface fluctuations/deformations can be subject to non-negligible scale effects for the present range of Reynolds numbers. The scale effects result in underestimated bubble count rate and biased bubble size distributions in the model, which has been confirmed by Bai et al. (2021) and Wang et al. (2023) in recent prototype hydraulic jump studies. Similarly, in a prototype A-jump with much larger Reynolds and Weber numbers, a substantially increasing number of small-sized bubbles would be entrained, convected and diffused in the water flow, leading to stronger air–water mixing than that was observed in the model. In this sense, the step cavity region may be better aerated with small bubbles entrapped in and carried by coherent vortical structures. On the other hand, the intruding jet thickness in the present hydraulic jump models was fairly small, allowing for active exchange of air bubbles between the upper aerated flow (e.g. for $y > s$) and the bottom roller ($0 < y < s$) in the step cavity. However, in a prototype A-jump with large approach flow depth, the air entrained on the top surface of the jet would not be able to easily cross the jet clear-water core to reach the bottom roller. How the bottom roller flow field interacts with the entrained air in full-scale A-jumps needs further clarification, probably in efforts of field data collection with preinstalled instruments.

7 Conclusions

A-type hydraulic jumps over abrupt bottom drops were investigated experimentally for a range of inflow conditions ($F_1 = 4.07, 6.10, 7.64, 10.31$) and drop heights ($s/d_1 = 0, 0.87, 1.74, 3.48$). The comparative analysis revealed some influence of the abrupt drop on the free-surface and air entrainment properties. In addition to the stabilized jump position and increased conjugate depth over the lowered stilling basin bed, the free-surface measurement results highlighted comparatively longer jump lengths, flattened jump front steepness and weakened free-surface fluctuations with increasing drop height. The velocity measurements captured flow reversal in the bottom roller zone in the step cavity, where a secondary maximum void fraction and bubble count rate were shown. The theoretical velocity and void fraction distributions were adjusted accordingly in the bottom roller section, for which the characteristic positions of maximum velocity, local maximum void fraction and maximum bubble count rate all shifted downward with the deflected jet-shear flow. In comparison to the classic hydraulic jumps on a flat bed, the depth-averaged void fraction reduced with increasing drop height, while the dimensionless bubble diffusivity in the turbulent shear region increased. Differing from the comparable expansion rates of the bubble diffusion layer and turbulent

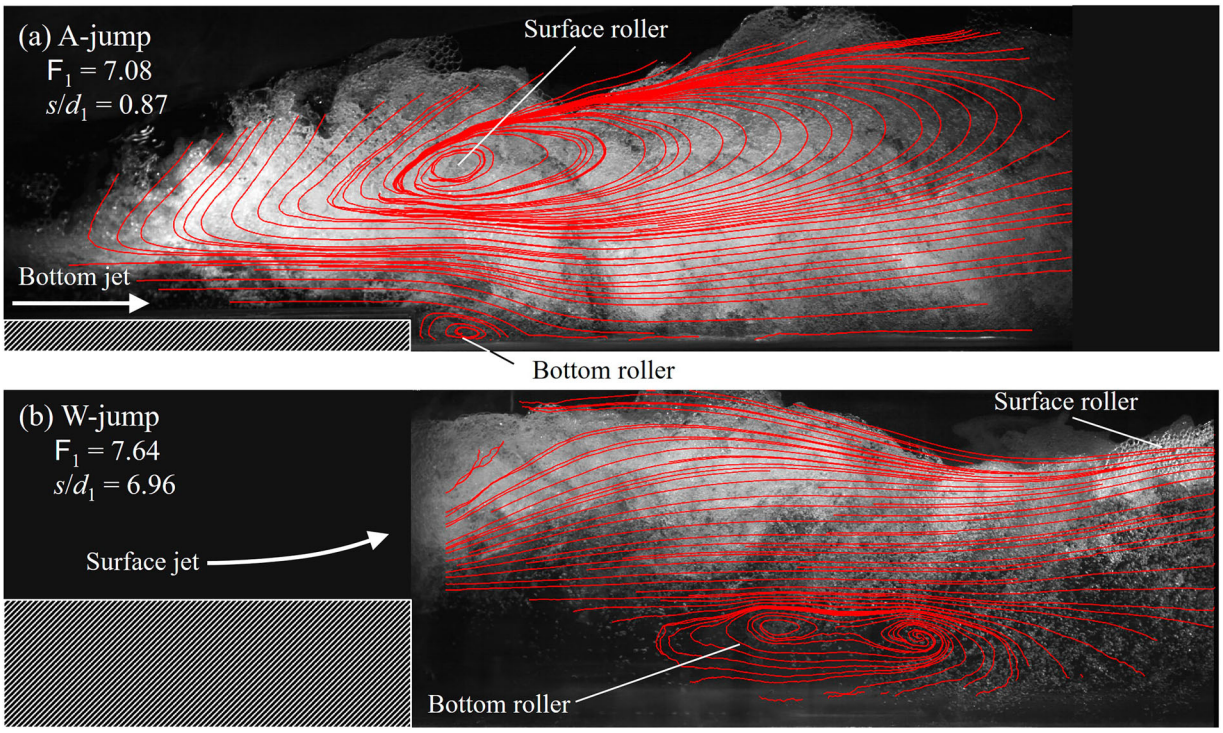

Figure 11 Optical flow visualization of streamline structures in (a) A-jump with $F_1 = 7.08$, $s/d_1 = 0.87$ and (b) W-jump with $F_1 = 7.64$, $s/d_1 = 6.96$. Red lines outline time-averaged streamlines comparing to an instantaneous shoot of air–water flow on background

shear layer in classic hydraulic jumps, the abrupt drop caused a faster broadening of the diffusion layer than the shear flow downstream of the step. A minor local increasing bubble count rate was noticed for large Froude numbers due to the additional bubble breakup at the jet reattachment to the bottom. The interaction of the bottom roller with the entrained air bubbles should be further investigated with improved measurement resolution and accuracy, and the approach jet thickness can be particularly relevant at larger scales in addition to the known scale effects on air entrainment.

Appendix

A CHJ becomes an A-jump when a relatively small bottom drop presents below the surface roller. For the same flow rate and approach depth, a further increase in the drop height would lead to a transition from A-jump to W-jump. According to an additional test of $s = 0.16$ m, i.e. twice the largest drop height in Table 1, A-jumps could not hold for the Froude numbers and jump toe positions as in Table 1, due to the insufficient tailwater level above the lowered bottom. This is illustrated in Fig. 11 showing two sideview snapshots of the A-jump ($s/d_1 = 0.87$) and W-jump ($s/d_1 = 6.96$) with a similar distance from the jump toe to the drop edge. The flow visualization was achieved using a high-speed camera (Revealer™ X150, Hefei, China) at 2000 fps and a resolution of 2592 × 1920 pixels. The streamlines in Fig. 11 were derived from the optical flow field that was analysed with a self-programmed MATLAB code adopting similar algorithm as in Kramer and Valero (2020). The different flow structures of the two types of jumps are clearly outlined. Comparing to the typical A-jump configuration in Fig. 11a, the downstream water level of the W-jump in Fig. 11b could not hold the surface roller above the step, and the impinging jet was deflected upward by the large bottom roller behind the drop, forming a curved and self-aerated surface jet followed by a small plunging-like surface roller. A tailwater depth large enough to maintain an A-type jump would push the jump toe upstream until the entire surface roller lay on the top of the step. Visually, the near-bottom flow region beneath the W-jump was much less aerated than the A-jump of the same inflow conditions.

Notation

A = correlation screening parameter (–)
C = void fraction (–)
C_{max} = local maximum void fraction in the jet-shear region (–)
$C^b{}_{max}$ = local maximum void fraction in the bottom roller region (–)
C_{mean} = depth-averaged void fraction (–)
d_1 = approach flow depth (m)
d_2 = downstream conjugate depth (m)
$D_{\#}$ = dimensionless bubble diffusivity in the jet-shear region (–)

$D^b_{\#}$ = dimensionless bubble diffusivity in the bottom roller region (–)
D_* = dimensionless bubble diffusivity in the free-surface region (–)
F_1 = inflow Froude number (–)
F = bubble count rate (Hz)
$F_{\max}$ = maximum bubble count rate (Hz)
g = gravity acceleration (m s$^-\supset$2)
L_j = hydraulic jump length (m)
M_1 = momentum flux upstream of the jump (N m^{-1})
M_2 = momentum flux downstream of the jump (N m^{-1})
N_p = number of particle (–)
P_1 = integral pressure upstream of the jump (N m^{-1})
P_2 = integral pressure downstream of the jump (N m^{-1})
P_s = integral pressure on the vertical drop surface (N m^{-1})
s = abrupt drop height (m)
Q = flow rate (m^3 s^{-1})
R_1 = Reynolds number (–)
V_1 = mean approach velocity (m s^{-1})
$V_{\max}$ = maximum velocity (m s^{-1})
$V^b{}_{\max}$ = local maximum reversing velocity magnitude in the bottom roller (m s^{-1})
V_{fs} = average velocity across the upper free-surface region (m s^{-1})
W = channel width (m)
W = Weber number (–)
x = longitudinal distance from the upstream nozzle outlet (m)
x_1 = longitudinal distance from the upstream nozzle outlet to the mean jump toe position (m)
x_s = longitudinal distance from the upstream nozzle outlet to the abrupt drop (m)
y = vertical distance from the bottom (m)
$y_{C\max}$ = vertical location of $C_{\max}$ (m)
$y^b{}_{C\max}$ = vertical location of $C^b{}_{\max}$ (m)
$y_{V\max}$ = vertical location of $V_{\max}$ (m)
$y^b{}_{V\max}$ = vertical location of $V^b{}_{\max}$ (m)
$y_{0.5}$ = vertical location where $V = (V_{\max} + V_{fs})/2$ (m)
$y^b{}_{0.5}$ = vertical location where $V = (V_{\max} + V^b{}_{\max})/2$ (m)
y_{90} = vertical location where $C = 0.9$ (m)
α = jump front slope (°)
η = free-surface elevation above the bottom level (m)
η' = characteristic free-surface fluctuation magnitude (m)
$\eta'_{\max}$ = maximum free-surface fluctuation (m)
σ = the surface tension (N m^{-1})
ν = kinematic viscosity of water (m^2 s^{-1})

Acknowledgement

The assistance of Rongcai Tang with the optical flow analysis is acknowledged.

Disclosure statement

No potential conflict of interest was reported by the author(s).

Funding

This work was supported the National Natural Science Foundation of China [grant no. 52192673, 51939007] and the Natural Science Foundation of Sichuan Province [grant no. 2022NSFSC0970].

References

Armenio, V., Toscano, P., & Fiorotto, V. (2000). On the effects of a negative step in pressure fluctuations at the bottom of a hydraulic jump. *Journal of Hydraulic Research*, *38*(5), 359–368. https://doi.org/10.1080/00221680009498317

Bai, Z., Bai, R., Tang, R., Wang, H., & Liu, S. (2021). Case study of prototype hydraulic jump on slope: air entrainment and free-surface measurement. *Journal of Hydraulic Engineering*, *147*(9), 05021007. https://doi.org/10.1061/(ASCE)HY.1943-7900.0001916

Bowers, C. E., & Toso, J. (1990). Karnafuli project, model studies of spillway damage. *Journal of Hydraulic Engineering*, *114*(5), 469–483. https://doi.org/10.1061/(ASCE)0733-9429(1988)114:5(469)

Chanson, H. (2002). Air–water measurements with intrusive phase–detection probes: Can we improve their interpretation? *Journal of Hydraulic Engineering*, *128*(3), 252–255. https://doi.org/10.1061/(ASCE)0733-9429(2002)128:3(252)

Chanson, H. (2010). Convective transport of air bubbles in strong hydraulic jumps. *International Journal of Multiphase Flow*, *36*(10), 798–814. https://doi.org/10.1016/j.ijmultiphaseflow.2010.05.006

Chanson, H. (2011). Bubbly two-phase flow in hydraulic jumps at large Froude numbers. *Journal of Hydraulic Engineering*, *137*(4), 451–460. https://doi.org/10.1061/(ASCE)HY.1943-7900.0000323

Chen, J. G., Zhang, J. M., Xu, W. L., & Peng, Y. (2014). Characteristics of the velocity distribution in a hydraulic jump stilling basin with five parallel offset jets in a twin-layer configuration. *Journal of Hydraulic Engineering*, *140*(2), 208–217. https://doi.org/10.1061/(ASCE)HY.1943-7900.0000817

Crowe, C., Sommerfeld, M., & Tsuji, Y. (1998). *Multiphase flows with droplets and particles*. CRC Press.

De Padova, D., & Mossa, M. (2021). Hydraulic jump: a brief history and research challenges. *Water*, *13*(13), 1733. https://doi.org/10.3390/w13131733

De Padova, D., Mossa, M., & Sibilla, S. (2018). SPH numerical investigation of the characteristics of an oscillating hydraulic jump at an abrupt drop. *Journal of Hydrodynamics*, *30*(1), 106–113. https://doi.org/10.1007/s42241-018-0011-z

Felder, S., Montano, L., Cui, H., Peirson, W., & Kramer, M. (2021). Effect of inflow conditions on the free-surface properties of hydraulic jumps. *Journal of Hydraulic Research*, *59*(6), 1004–1017. https://doi.org/10.1080/00221686.2020.1866692

Ferreri, G. B., & Nasello, C. (2002). Hydraulic jumps at drop and abrupt enlargement in rectangular channel. *Journal of Hydraulic Research*, *40*(4), 491–505. https://doi.org/10.1080/00221680209499891

Gualtieri, C., & Chanson, H. (2007). Experimental analysis of Froude number effect on air entrainment in the hydraulic jump. *Environmental Fluid Mechanics*, *7*(3), 217–238. https://doi.org/10.1007/s10652-006-9016-1

Gualtieri, C., & Chanson, H. (2021). Physical and numerical modelling of air-water flows: An introductory overview. *Environmental Modelling & Software*, *143*, 105109. https://doi.org/10.1016/j.envsoft.2021.105109

Hager, W. H. (1992). *Energy dissipators and hydraulic jump*. Kluwer Academic Publishers.

Hager, W. H., & Bretz, N. V. (1986). Hydraulic jumps at positive and negative steps. *Journal of Hydraulic Research*, *24*(4), 237–253. https://doi.org/10.1080/00221688609499303

Kawagoshi, N., & Hager, W. H. (1990a). Hydraulic jumps at rounded drop. *Proceedings of the Institution of Civil Engineers*, Part 2, *89*(4), 443–470.

Kawagoshi, N., & Hager, W. H. (1990b). Wave type flow at abrupt drops. *Journal of Hydraulic Research*, *28*(2), 235–252. https://doi.org/10.1080/00221689009499088

Kramer, M., & Valero, D. (2020). Turbulence and self-similarity in highly aerated shear flows: the stable hydraulic jump. *International Journal of Multiphase Flow*, *129*, 103316. https://doi.org/10.1016/j.ijmultiphaseflow.2020.103316

Kramer, M., Valero, D., Chanson, H., & Bung, D. B. (2019). Towards reliable turbulence estimations with phase-detection probes: an adaptive window cross-correlation technique. *Experiments in Fluids*, *60*(1), 2. https://doi.org/10.1007/s00348-018-2650-9

Kramer, M., Hohermuth, B., Valero, D., & Felder, S. (2020). Best practices for velocity estimations in highly aerated flows with dual-tip phase-detection probes. *International Journal of Multiphase Flow*, *126*, 103228. https://doi.org/10.1016/j.ijmultiphaseflow.2020.103228

Kucukali, S., & Chanson, H. (2008). Turbulence measurements in hydraulic jumps with partially-developed inflow conditions. *Experimental Thermal and Fluid Science*, *33*(1), 41–53. https://doi.org/10.1016/j.expthermflusci.2008.06.012

Montano, L., & Felder, S. (2021). Air-water flow properties in hydraulic jumps with fully and partially developed inflow conditions. *Journal of Fluids Engineering*, *143*(10), 101403. https://doi.org/10.1115/1.4051199

Moore, W. L., & Morgan, C. W. (1959). Hydraulic jump at an abrupt drop. *Trans. ASCE*, *124*(2991), 507–524. https://doi.org/10.1061/JYCEAJ.0000146

Mossa, M., Petrillo, A., & Chanson, H. (2003). Tailwater level effects on flow conditions at an abrupt drop. *Journal of Hydraulic Research*, *41*(1), 39–51. https://doi.org/10.1080/00221680309499927

Murzyn, F., & Chanson, H. (2009). Experimental investigation of bubbly flow and turbulence in hydraulic jumps. *Environmental Fluid Mechanics*, *9*(2), 143–159. https://doi.org/10.1007/s10652-008-9077-4

Murzyn, F., Mouaze, D., & Chaplin, J. R. (2007). Air-water interface dynamic and free surface features in hydraulic jumps. *Journal of Hydraulic Research*, *45*(5), 679–685. https://doi.org/10.1080/00221686.2007.9521804

Ohtsu, I., & Yasuda, Y. (1991). Transition from supercritical to subcritical flow at an abrupt drop. *Journal of Hydraulic Research*, *29*(3), 309–328. https://doi.org/10.1080/00221689109498436

Rajaratnam, N., & Ortiz, N. V. (1977). Hydraulic jumps and waves at abrupt drops. *Journal of Hydraulic Division*, *103*(4), 381–394. https://doi.org/10.1061/JYCEAJ.0004732

Stojnic, I., Pfister, M., Matos, J., & Schleiss, A. (2021). Effect of 30-degree sloping smooth and stepped chute approach flow on the performance of a classic stilling basin. *Journal of Hydraulic Engineering*, *147*(2), 04020097. https://doi.org/10.1061/(ASCE)HY.1943-7900.0001840

Toombes, L., & Chasnson, H. (2007). Free-surface aeration and momentum exchange at a bottom outlet. *Journal of Hydraulic Research*, *45*(1), 100–110. https://doi.org/10.1080/00221686.2007.9521748

Valero, D., Chanson, H., & Bung, D. B. (2020). Robust estimators for free surface turbulence characterization: a stepped spillway application. *Flow Measurement and Instrumentation*, *76*, 101809. https://doi.org/10.1016/j.flowmeasinst.2020.101809

Wang, H. (2014). *Turbulence and air entrainment in hydraulic jumps* [Ph.D. thesis]. School of Civil Engineering, The University of Queensland, Australia. https://espace.library.uq.edu.au/view/UQ:345033.

Wang, H., & Chanson, H. (2015). Experimental study of turbulent fluctuations in hydraulic jumps. *Journal of Hydraulic Engineering*, *141*(7), 04015010. https://doi.org/10.1061/(ASCE)HY.1943-7900.0001010

Wang, H., & Chanson, H. (2016). Self-similarity and scale effects in physical modelling of hydraulic jump roller dynamics, air entrainment and turbulent scales. *Environmental Fluid Mechanics*, *16*(6), 1087–1110. https://doi.org/10.1007/s10652-016-9466-z

Wang, H., Liu, X., Bai, R., & Liu, S. (2021). Bubble characteristics affecting air-water exchange in open-channel flow with a jet forming over a sudden bottom drop. *Experimental Thermal and Fluid Science*, *124*, 110366. https://doi.org/10.1016/j.expthermflusci.2021.110366

Wang, H., Tang, R., Bai, Z., Liu, S., Sang, W., & Bai, R. (2023). Prototype air-water flow measurements in D-

type hydraulic jumps. *Journal of Hydraulic Research*, *61*(1), 145–161. https://doi.org/10.1080/00221686.2022.2132310

Wüthrich, D., Shi, R., & Chanson, H. (2022). Hydraulic jumps with low inflow Froude numbers: air–water surface patterns and transverse distributions of two-phase flow properties. *Environmental Fluid Mechanics*, https://doi.org/10.1007/s10652-022-09854-5

Zhang, G., Valero, D., Bung, D. B., & Chanson, H. (2018). On the estimation of free-surface turbulence using ultrasonic sensors. *Flow Measurement and Instrumentation*, *60*, 171–184. https://doi.org/10.1016/j.flowmeasinst.2018.02.009

Zhao, W., Xu, W., Wang, H., Tang, R., & Bai, R. (2023). Roller fluctuations of pre-aerated high-Froude-number hydraulic jumps. *Proceedings of the Institution of Civil Engineers - Water Management*. https://doi.org/10.1680/jwama.21.00046